

TESS first look at evolved compact pulsators

Asteroseismology of the pulsating helium-atmosphere white dwarf TIC 257459955

Keaton J. Bell^{1,2}, Alejandro H. Córdoba^{3,4}, Agnès Bischoff-Kim⁵, Leandro G. Althaus^{3,4}, P. A. Bradley⁶,
Leila M. Calcaferro^{3,4}, M. H. Montgomery⁷, Murat Uzundag⁸, Andrzej S. Baran⁹, Zs. Bognár^{10,11}, S. Charpinet¹²,
H. Ghasemi¹³, and J. J. Hermes¹⁴

¹ Max-Planck-Institut für Sonnensystemforschung (MPS), Justus-von-Liebig-Weg 3, 37077 Göttingen, Germany
e-mail: bell@mps.mpg.de

² Department of Physics and Astronomy, Stellar Astrophysics Centre, Aarhus University, Ny Munkegade 120, 8000 Aarhus C, Denmark

³ Grupo de Evolución Estelar y Pulsaciones. Facultad de Ciencias Astronómicas y Geofísicas, Universidad Nacional de La Plata, Paseo del Bosque s/n, 1900 La Plata, Argentina

⁴ IALP - CONICET

⁵ Penn State Worthington Scranton, Dunmore, PA 18512, USA

⁶ XCP-6, MS F-699 Los Alamos National Laboratory, Los Alamos, NM 87545, USA

⁷ Department of Astronomy, University of Texas at Austin, Austin, TX - 78712, USA

⁸ Instituto de Física y Astronomía, Universidad de Valparaíso, Gran Bretaña 1111, Playa Ancha, Valparaíso 2360102, Chile

⁹ Uniwersytet Pedagogiczny, Obserwatorium na Suhorze, ul. Podchorążych 2, 30-084 Kraków, Polska

¹⁰ Konkoly Observatory, MTA Research Centre for Astronomy and Earth Sciences, Konkoly Thege Miklós út 15-17, H-1121, Budapest, Hungary

¹¹ MTA CSFK Lendület Near-Field Cosmology Research Group

¹² Institut de Recherche en Astrophysique et Planétologie, CNRS, Université de Toulouse, CNES, 14 avenue Edouard Belin, F-31400 Toulouse, France

¹³ Department of Physics, Institute for Advanced Studies in Basic Sciences (IASBS), Zanjan 45137-66731, Iran

¹⁴ Department of Astronomy, Boston University, 725 Commonwealth Ave., Boston, MA 02215, USA

ABSTRACT

Context. Pulsation frequencies reveal the interior structures of white dwarf stars, shedding light on the properties of these compact objects that represent the final evolutionary stage of most stars. Two-minute cadence photometry from the Transiting Exoplanet Survey Satellite (*TESS*) will record pulsation signatures from bright white dwarfs over the entire sky.

Aims. As part of a series of first-light papers from *TESS* Asteroseismic Science Consortium Working Group 8, we aim to demonstrate the sensitivity of *TESS* data to measuring pulsations of helium-atmosphere white dwarfs in the DBV instability strip, and what asteroseismic analysis of these measurements can constrain about their stellar structures. We present a case study of the pulsating DBV WD 0158–160 that was observed as TIC 257459955 with the 2-minute cadence for 20.3 days in *TESS* Sector 3.

Methods. We measure the frequencies of variability of TIC 257459955 with an iterative periodogram and prewhitening procedure. The measured frequencies are compared to calculations from two sets of white dwarf models to constrain the stellar parameters: the fully evolutionary models from LPCODE, and the structural models from WDEC.

Results. We detect and measure the frequencies of nine pulsation modes and eleven combination frequencies of WD 0158–160 to $\sim 0.01 \mu\text{Hz}$ precision. Most, if not all, of the observed pulsations belong to an incomplete sequence of dipole ($\ell = 1$) modes with a mean period spacing of 38.1 ± 1.0 s. The best-fit seismic models from both LPCODE and WDEC have effective temperatures that are ≥ 3000 K hotter than the archival spectroscopic value of 25,500 K. These hotter solutions give a seismic distance that is in better agreement with the *Gaia* parallax.

Conclusions. Our results demonstrate the value of the *TESS* data for DBV white dwarf asteroseismology. The extent of the short-cadence photometry enables reliably accurate and extremely precise pulsation frequency measurements. Having found consistent subsets of both the LPCODE and WDEC models that show good agreement with the measured pulsation periods, we can proceed with these methods to asteroseismically constrain the global and interior properties of additional DBVs observed by *TESS* with confidence.

Key words. asteroseismology – stars: oscillations – stars: variables: general – white dwarfs

1. Introduction

The Transiting Exoplanet Survey Satellite (*TESS*) is a NASA mission with the primary goal of detecting exoplanets that transit the brightest and nearest stars (Ricker et al. 2014). More generally, the extensive time series photometry that *TESS* acquires

is valuable for studying a wide variety of processes that cause stars to appear photometrically variable. One particularly powerful use for these data is to constrain the global properties and interior structures of pulsating stars with the methods of asteroseismology. Pulsating stars oscillate globally in standing waves

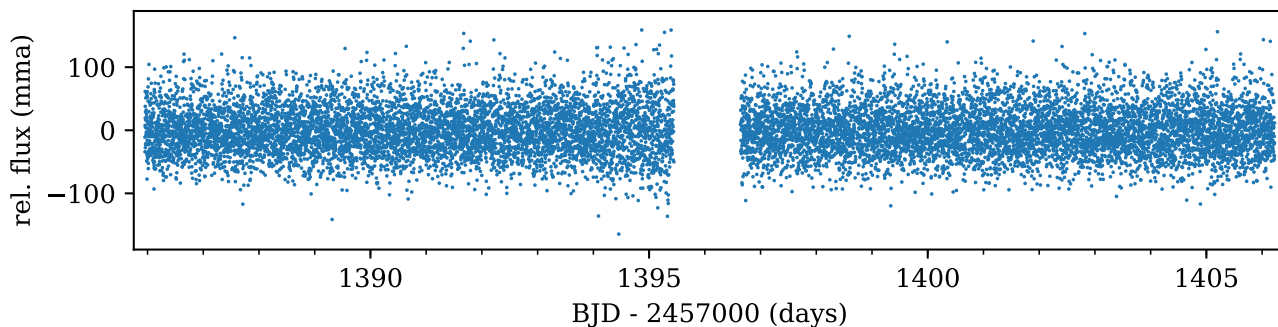


Fig. 1. Final reduced *TESS* Sector 3 light curve of TIC 257459955. A gap occurs at spacecraft perigee.

that propagate through and are affected by the stellar interiors. Fourier analysis of the light curves of pulsating stars reveals their eigenfrequencies that can be compared to calculations from stellar models, providing the most sensitive technique for probing stellar interior structures.

The *TESS* Asteroseismic Science Consortium (TASC) is a collaboration of the scientific community that shares an interest in utilizing *TESS* data for asteroseismology research. It is organized into a number of working groups that address different classes of stars. TASC Working Group 8 (WG8) focuses on *TESS* observations of evolved compact stars that exhibit photometric variability, including hot subdwarfs, white dwarf stars, and pre-white dwarfs. To this goal, WG8 has proposed for all known and likely compact stars with *TESS* magnitudes $\lesssim 16$ to be observed at the short, 2-minute cadence.

Within TASC WG8, the subgroup WG8.2 coordinates the studies of pulsating white dwarfs observed by *TESS*. Depending on their atmospheric compositions, white dwarfs may pulsate as they cool through three distinct instability strips: DOVs (GW Vir stars or pulsating PG 1159 stars) are the hottest and include some central stars of planetary nebulae; DBVs (V777 Her stars) have helium atmospheres that are partially ionized in the effective temperature range $32,000 \geq T_{\text{eff}} \geq 22,000$ K, driving pulsations; and DAVs (ZZ Ceti stars) pulsate when their pure-hydrogen atmospheres are partially ionized from $12,500 \geq T_{\text{eff}} \geq 10,800$ K (at the canonical mass of $\approx 0.6 M_{\odot}$). Pulsations of these objects probe the physics of matter under the extreme pressures of white dwarf interiors. Since white dwarfs are the final products of $\approx 97\%$ of Galactic stellar evolution, asteroseismic determination of their compositions and structures probes the physical processes that operate during previous evolutionary phases. See Winget & Kepler (2008), Fontaine & Brassard (2008), and Althaus et al. (2010) for reviews of the field of white dwarf asteroseismology, and Córscico et al. (2019) for coverage of the most recent decade of discovery in the era of extensive space-based photometry from *Kepler* and *K2*.

As part of the initial activities of the TASC WG8.2, we present analyses of examples of each type of pulsating white dwarf observed at 2-minute cadence in the first *TESS* Sectors in a series of first light papers. These follow the initial TASC WG8 first-light analysis of a pulsating hot subdwarf in *TESS* data from Charpinet et al. (2019, submitted). In this paper, we study the DBV pulsator WD 0158–160 (also EC 01585–1600), which was observed by *TESS* as target TIC 257459955 in Sector 3. Voss et al. (2007) confirm the classification of WD 0158–160 as a DB (helium-atmosphere) white dwarf from a ESO Supernova type Ia Progenitor survey (SPY) spectrum and measure atmospheric parameters of $T_{\text{eff}} = 25,518$ K and $\log g = 7.875$. Astrometric parallax from *Gaia* DR2 (Gaia Collaboration et al. 2016, 2018)

place WD 0158–160 at a distance of 68.14 ± 0.28 pc (Bailer-Jones et al. 2018). This is one of the brightest DBVs known ($B = 14.59$ mag; Zacharias et al. 2012) and was discovered to be a variable recently by Kilkenny (2016). They obtained high-speed photometry on the Sutherland 1-meter telescope of the South African Astronomical Observatory over five nights, measuring ten frequencies of significant variability between 1285–5747 μHz . We aim to measure more precise pulsation frequencies from the *TESS* data and to compare these with stellar models to asteroseismically constrain the properties of this DB white dwarf.

2. *TESS* data

TIC 257459955 was observed at the short, 2-minute cadence by *TESS* in Sector 3, which collected 20.3 days of useful data with a 1.12-day gap at spacecraft perigee.¹ Light curves from this particular Sector are shorter than the nominal 27-day duration, and the periodogram achieves a correspondingly lower frequency resolution and signal-to-noise than expected for most *TESS* observations. Thus, *TESS*'s value for asteroseismology of white dwarfs observed in Sectors with longer coverage is typically greater than demonstrated in this paper.

We use the 2-minute short-cadence *TESS* light curve of TIC 257459955 that has had common instrumental trends removed by the Pre-Search Data Conditioning Pipeline (PDC; Stumpe et al. 2012) that we downloaded from MAST.² We discard two observations that have quality flags set by the pipeline. We do not identify any additional outlying measurements that need to be removed. The final light curve contains 13,450 measurements that span 20.27 days.

To remove any additional low-frequency systematics from the light curve, we divide out the fit of a fourth-order Savitzky–Golay filter with a three-day window length computed with the Python package `LIGHTKURVE` (Barentsen et al. 2019). This preserves the signals from pulsations that typically have periods of $\lesssim 20$ -min in white dwarfs. The final reduced light curve is displayed in Figure 1, where the relative flux unit of milli-modulation amplitude (mma) equals 0.1% flux variation or one part-per-thousand. The root-mean-squared scatter of the flux measurements is 37.8 mma (3.78%).

3. Frequency solution

Asteroseismology relies on the precise determination of pulsation frequencies. We benefit from the length of the *TESS* data provid-

¹ See *TESS* Data Release Notes: http://archive.stsci.edu/tess/tess_drn.html

² <https://archive.stsci.edu/>

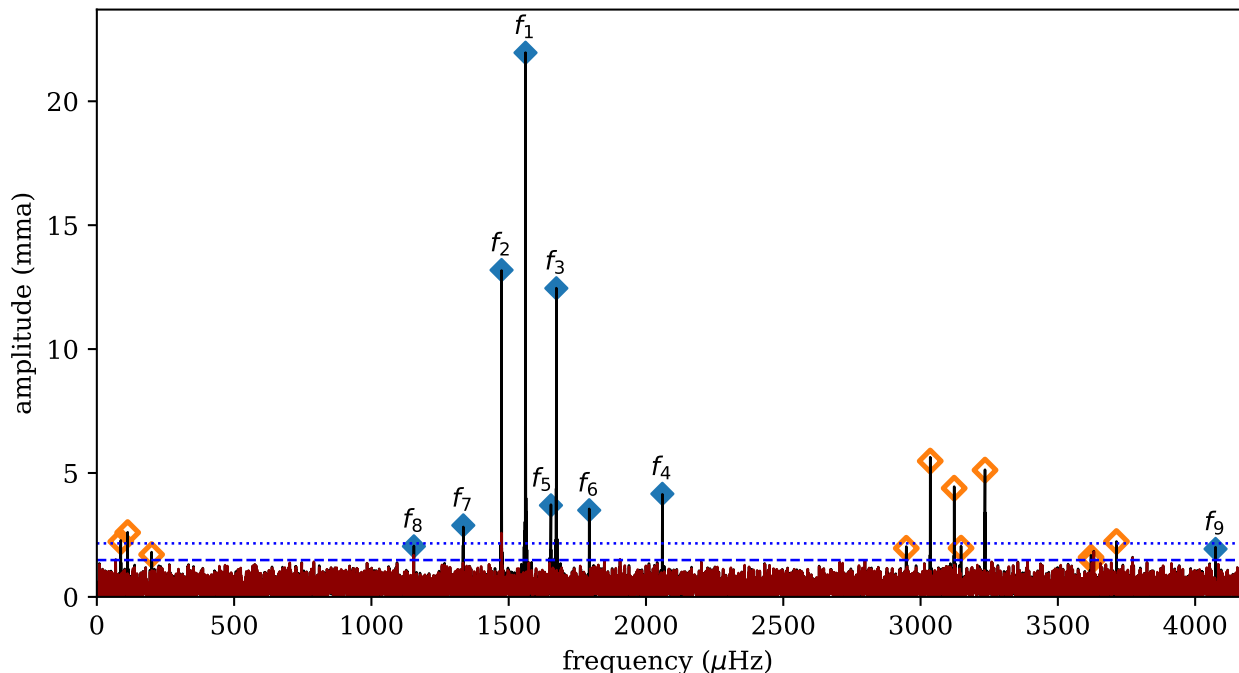


Fig. 2. Lomb-Scargle periodogram of the original TIC 257459955 light curve (black) and of the residuals after subtracting off the best fit frequency solution (red). The dotted horizontal line shows the final 0.1% false-alarm-probability (FAP) significance threshold for the residual spectrum, and the dashed line is a 0.1% FAP level for an individual frequency bin. Blue filled diamonds mark the best-fit frequencies and amplitudes of independent modes, and orange, unfilled diamonds mark combination frequencies. Independent modes are labeled with mode IDs from Table 1.

Table 1. Pulsational frequency solution from the *TESS* light curve of TIC 257459955. The independent pulsation modes are listed first in order of decreasing amplitude, followed by all identified combination frequencies.

mode ID	frequency (μHz)	period (s)	amplitude (mma)
f_1	1561.200 ± 0.005	640.533 ± 0.002	22.0 ± 0.4
f_2	1473.985 ± 0.008	678.433 ± 0.004	13.2 ± 0.4
f_3	1673.490 ± 0.008	597.554 ± 0.003	12.5 ± 0.4
f_4	2059.62 ± 0.02	485.527 ± 0.006	4.2 ± 0.4
f_5	1653.87 ± 0.03	604.642 ± 0.010	3.7 ± 0.4
f_6	1793.24 ± 0.03	557.649 ± 0.010	3.5 ± 0.4
f_7	1334.64 ± 0.04	749.27 ± 0.02	2.9 ± 0.4
f_8	1154.77 ± 0.06	865.97 ± 0.04	2.0 ± 0.4
f_9	4074.32 ± 0.06	245.440 ± 0.004	1.9 ± 0.4
$f_1 - f_2$	87.215 ± 0.009	11466.0 ± 1.2	2.23 ± 0.4
$f_3 - f_1$	112.290 ± 0.010	8905.5 ± 0.8	2.60 ± 0.4
$f_3 - f_2$	199.504 ± 0.011	5012.4 ± 0.3	1.71 ± 0.4
$2f_1$	3122.400 ± 0.009	320.267 ± 0.001	4.39 ± 0.4
$2f_2$	2947.971 ± 0.015	339.2164 ± 0.0017	1.97 ± 0.4
$f_1 + f_2$	3035.185 ± 0.009	329.4692 ± 0.0009	5.5 ± 0.4
$f_1 + f_3$	3234.690 ± 0.009	309.1487 ± 0.0009	5.1 ± 0.4
$f_1 + f_4$	3620.82 ± 0.02	276.1809 ± 0.0018	1.6 ± 0.4
$f_2 + f_3$	3147.475 ± 0.011	317.7150 ± 0.0011	2.0 ± 0.4
$f_4 + f_5$	3713.49 ± 0.03	269.289 ± 0.002	2.2 ± 0.4
$f_1 + f_2 + f_3$	4708.675 ± 0.012	212.3740 ± 0.0005	1.5 ± 0.4

ing a high frequency resolution of $0.57 \mu\text{Hz}$ (inverse of the light curve duration) without complications from aliasing that would arise from large gaps in the time series. We use the fast Lomb-Scargle implementation in *astropy* (Astropy Collaboration et al. 2018) to compute periodograms of the unweighted time series photometry. We oversample the natural frequency resolution by a factor of 10 so that the periodogram peaks more accurately

represent the intrinsic frequencies and amplitudes of the underlying signals. The full periodogram out to the Nyquist frequency of $4166.59 \mu\text{Hz}$ is displayed in black in Figure 2.

Including any noise peaks in our frequency solution would adversely affect our asteroseismic inferences, so we adopt a conservative significance criterion for signal amplitudes. We test the null hypothesis that the highest peak in the periodogram is

caused by pure noise by treating the observed flux measurements in the light curve as a proxy for the noise distribution. We bootstrap a significance threshold by generating 10,000 pure-noise time series that sample from this distribution with replacement at the observation times of the original light curve. The 99.9th highest percentile corresponds to a false alarm probability (FAP) of 0.1% that a peak with a higher amplitude anywhere in the oversampled periodogram is caused by noise alone. We have high confidence that peaks above this threshold correspond to significant signals. For our initial periodogram, we find that peaks with amplitudes above 2.71 mma (4.7 times the mean noise level in the periodogram³) have $\text{FAP} < 0.1\%$.

We adopt frequencies into our solution according to an iterative prewhitening procedure. We record the frequencies and amplitudes of every peak above our 0.1% FAP significance threshold. These provide initial values for a multi-sinusoid fit to the time series data,⁴ which we compute with the non-linear least-squares minimization Python package `lmfit` (Newville 2018). Frequencies that agree within the natural frequency resolution with a sum, integer multiple, or difference between higher-amplitude signals are identified as combination frequencies. These arise from a nonlinear response of the flux to the stellar pulsations (Brickhill 1992), and we enforce a strict arithmetic relationship between these combinations frequencies and the parent pulsation frequencies when performing the fit. Including the combination frequencies slightly improves the measurement precision of the parent mode frequencies. Once all significant signals are included in our model and fitted to the time series, we subtract off the model and repeat the process on the residuals, starting by recalculating the periodogram and bootstrapping its 0.1% FAP significance threshold. This is repeated until no further signals meet our acceptance criterion.

At this point, the periodogram still exhibits a few compelling peaks at locations where we specifically expect that signals might appear. For assessing significance in these cases, we bootstrap a different 0.1% FAP threshold for the amplitude of a peak within a single frequency bin (as opposed to considering the highest peak anywhere in the entire spectrum). We adopt signals that correspond to combinations of accepted modes into our solution that exceed this lower threshold. We accept another independent pulsation mode at $1154.77 \pm 0.06 \mu\text{Hz}$ (f_8 in Table 1) that closely matches the asymptotic mean period spacing of $\ell = 1$ modes that we identify in our preliminary asteroseismic mode identification in Section 4.1. We also include the peak at $4074.32 \pm 0.06 \mu\text{Hz}$ (f_9) as an intrinsic pulsation mode since it agrees with the measurement of a frequency at $4074.0 \pm 0.1 \mu\text{Hz}$ from the ground-based discovery data of Kilkeny (2016) to within the periodogram frequency resolution. After prewhitening these signals, the final single-bin significance threshold is at 1.50 mma,⁵ compared to the 0.1% FAP level across the entire spectrum at 2.24 mma.

The final best-fit values for the frequencies (periods) and amplitudes of the individual sinusoids in our model are given in Table 1. The quoted errors are estimated by `lmfit` from the covariance matrix, and they agree with expectations from an-

³ This matches the significance threshold advocated for by Baran et al. (2015), though they use a different method to arrive at this level, interpreting it as the threshold that yields the correct frequency determinations in 95% of random realizations.

⁴ Our interactive Python-based periodogram and sine-fitting code is available at <https://github.com/keatonb/Pyriod>.

⁵ The peak corresponding to the sub-Nyquist alias of the $f_1 + f_2 + f_3$ combination frequency exceeded this threshold even though the best-fit amplitude in the final solution is lower.

alytical formulae for the independent modes (Montgomery & O’Donoghue 1999). In Figure 2, the dotted line indicates the final full-spectrum 0.1% FAP significance threshold and the dashed line marks the lower per-bin threshold. These values are indicated by diamond markers (independent modes in filled blue and combination frequencies in unfilled orange). The periodogram of the final residuals is displayed in red. The measured amplitudes will generally be lower than the intrinsic disc-integrated amplitudes due to smoothing from the 2-minute exposures. The intrinsic frequency of the combination $f_1 + f_2 + f_3$ is above the observational Nyquist frequency, so we mark the corresponding alias peak near $3624.5 \mu\text{Hz}$.

There remain conspicuous low-amplitude peaks in the prewhitened periodogram that are adjacent to the f_2 and f_8 frequencies. These are likely caused by these signals exhibiting slight amplitude or phase variations during the *TESS* observations. The best-fit frequency values in Table 1 correspond to the highest and central peaks of each mode’s power that best represent the intrinsic pulsation frequencies, though the measured amplitudes may be less than the instantaneous maximum amplitudes of these signals during the observations.

4. Asteroseismic analyses

As a collaborative effort of the TASC WG8.2, all members with asteroseismic tools and models suited for this data set were invited to contribute their analyses. Two groups submitted full asteroseismic analyses to this effort, which we present in this section. This is the first direct comparison between asteroseismic analyses of the La Plata and Texas groups. By including multiple analyses, we aim to assess the consistency of asteroseismic inferences for pulsating DBVs that utilize different models and methods.

Owing to the quality of the space-based data, the measurements of pulsation mode frequencies presented in Table 1 are reliably accurate and extremely precise. Both analyses that follow aim to interpret this same set of pulsation frequency measurements. Certainly the sensitivity of the set of modes detected to the detailed interior structure is a primary limitation on our ability to constrain the properties of this particular DBV.

The combination frequencies are not considered in these analyses, since these are not eigenfrequencies of the star and do not correspond to the pulsation frequencies calculated for stellar models. This highlights the importance of identifying combination frequencies as such; erroneously requiring a model frequency to match a combination frequency would derail any asteroseismic inference.

4.1. Preliminary mode identification

Identifying common patterns in the pulsation spectrum can guide our comparison of the measured frequencies to stellar models. Gravity(*g*)-mode pulsations of white dwarfs are non-radial oscillations of spherical harmonic eigenfunctions of the stars. We observe the integrated light from one hemisphere of a star, so geometric cancellation effects (Dziembowski 1977) typically restrict us to detecting only modes of low spherical degree, $\ell = 1$ or 2 (modes with one or two nodal lines along the surface). Modes can be excited in a sequence of consecutive radial orders, k , for each ℓ . In the asymptotic limit ($k \gg \ell$), gravity modes of consecutive radial overtone are evenly spaced in period (Tassoul et

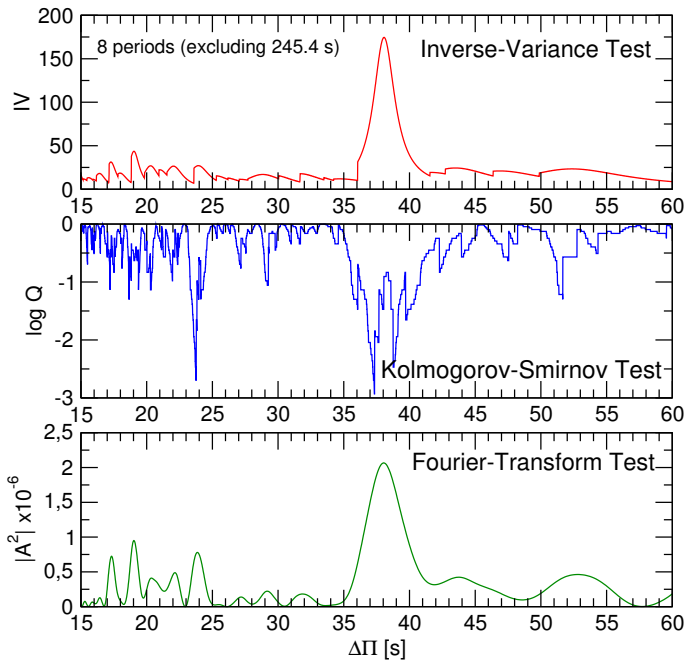


Fig. 3. I-V (upper panel), K-S (middle panel), and F-T (bottom panel) significance tests to search for a constant period spacing of TIC 257459955. The tests are applied to the pulsation periods in Table 1, excluding the 245.4 s period that is not clearly within the asymptotic regime. See text for details.

al. 1990), following approximately

$$\Pi_{\ell,k} \approx \Delta\Pi_{\ell}^a k + \epsilon = \frac{\Pi_0}{\sqrt{\ell(\ell+1)}} k + \epsilon, \quad (1)$$

where $\Delta\Pi_{\ell}^a$ is the period spacing, Π_0 and ϵ are constants.

We searched for a constant period spacings in the data of TIC 257459955 using the Kolmogorov-Smirnov (K-S; see Kawaler 1988), the inverse variance (I-V; see O’Donoghue 1994) and the Fourier Transform (F-T; see Handler et al. 1997) significance tests. In the K-S test, the quantity Q is defined as the probability that the observed periods are randomly distributed. Thus, any uniform or at least systematically non-random period spacing in the period spectrum of the star will appear as a minimum in Q . In the I-V test, a maximum of the inverse variance will indicate a constant period spacing. Finally, in the F-T test, we calculate the Fourier transform of a Dirac comb function (created from a set of observed periods), and then we plot the square of the amplitude of the resulting function in terms of the inverse of the frequency. And once again, a maximum in the square of the amplitude will indicate a constant period spacing. In Figure 3 we show the results of applying the tests to the set of periods of Table 1, excluding the short-period f_9 that is not clearly within the asymptotic ($k \gg \ell$) regime. The three tests support the existence of a mean period spacing of about 38 s which corresponds to our expectations for a dipole ($\ell = 1$) sequence. Note that for $\ell = 2$, according to Eq. (1), one should find a spacing of periods of ~ 22 s, which is not observed in our analysis.⁶ By averaging the period spacing derived from the three statistical tests, we found $\Delta\Pi = 38.1 \pm 1.8$ s as an initial period spacing detection.

We initially obtained a nearly identical result using a frequency solution that did not include f_8 , as this peak did not exceed our independent significance threshold. Once the prelimi-

⁶ There is an indication of a $\Delta\Pi \sim 24$ s, that is a bit longer than the prediction for $\ell = 2$ ($\Delta\Pi \sim 22$ s), but only from the K-S test.

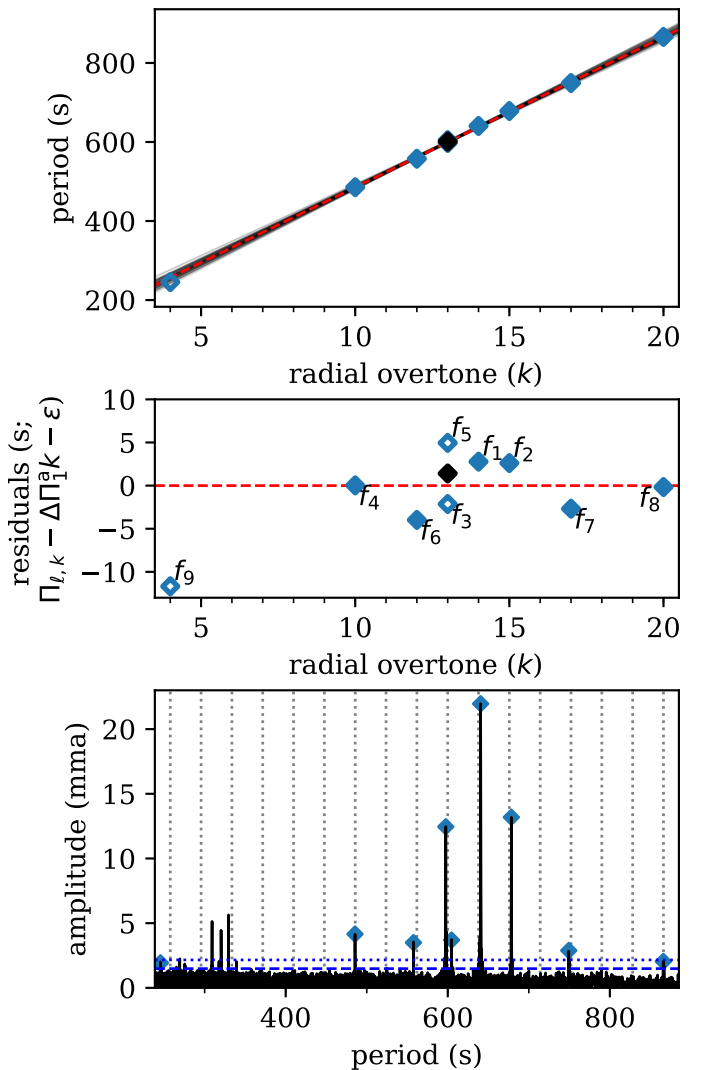


Fig. 4. Top: The independent pulsation periods of the star plotted versus radial overtone number k . The least-squares line fit to $k > 5$ (using the mean period of f_3 and f_5 for $k = 13$; black) indicates a roughly constant period spacing consistent with dipole $\ell = 1$ modes. The transparent gray lines represent fits to the perturbed periods assuming different observed azimuthal orders, m (see text). MIDDLE: Residuals of the linear fit shows evidence of a possible mode trapping cycle. We label the mode IDs from Table 1. Bottom: The pulsation spectrum in period space with the dotted vertical lines indicating the expected locations of $\ell = 1$ modes from the asymptotic pulsation theory given our least-squares fit parameters.

nary mode identifications were established, it became clear that f_8 is located precisely where we expect a $\ell = 1$ mode given the asymptotic period spacing. This prompted us to adopt this mode into our solution for exceeding the lower, frequency-dependent significance threshold, as described in Section 3.

This mean period spacing of the $\ell = 1$ modes cannot account for the signals at f_3 and f_5 that are separated by only $19.62 \pm 0.03 \mu\text{Hz}$ (7.088 ± 0.010 s). One of these could belong to the quadrupole ($\ell = 2$) sequence. Alternatively, f_3 and f_5 could both be components of a $\ell = 1$ rotational multiplet. Stellar rotation causes $2\ell + 1$ modes with different azimuthal orders, m , to exist for each pair of ℓ and k (where m is an integer between $-\ell$ and ℓ). These are separated evenly in frequency by an amount proportional to the stellar rotation rate (e.g., Cox 1984), though many may not be excited to observable amplitude. The frequency separation between f_3 and f_5 is within the range of rotational

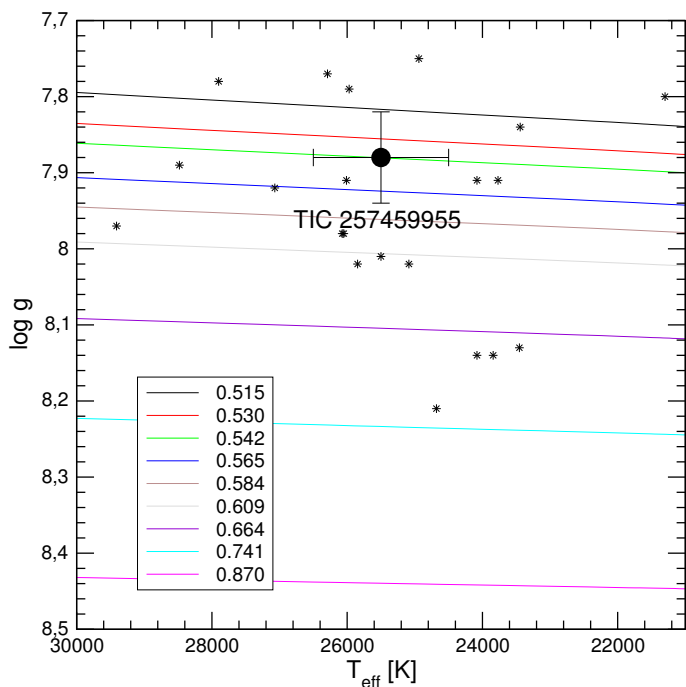


Fig. 5. Location of the known DBV stars on the $T_{\text{eff}}-\log g$ diagram (black star symbols) according to the compilation by Córscico et al. (2019, submitted). The DB white dwarf evolutionary tracks are depicted with different colours according to the stellar mass. Stellar masses are in solar units. The location of TIC 257459955 as given by spectroscopy (Voss et al. 2007) is highlighted with a large black circle and error bars. The stellar mass derived from linear interpolation is $M_{\star} = 0.542^{+0.028}_{-0.025} M_{\odot}$.

splittings of $\ell = 1$ modes detected from other pulsating white dwarfs in space-based data (e.g., Hermes et al. 2017b). We leave the exploration of alternate interpretations of these modes up to the individual analyses that follow.

The top panel of Figure 4 displays a least-squares fit of a line (Eq. 1) through the periods measured for the independent modes listed in Table 1, given the preliminary period spacing detected from our initial statistical tests. The modes follow a pattern that is consistent with an incomplete $\ell = 1$ sequence, though four consecutive modes are detected. The absolute radial overtone numbers, k , were obtained from the best period-by-period fits from both sets of models described in Sections 4.2 and 4.3. We exclude the mode f_9 from the fit because its low radial order ($k = 4$) is furthest from the asymptotic regime. Repeating the fit using alternatively f_3 and f_5 for the $k = 13$, $m = 0$ mode has a negligible effect on the best-fit parameters. The measured periods are weighted equally in the fits since uncertainty in the azimuthal order, m , and physical departures from even period spacing likely dominate over the tiny measurement errors⁷ in the residuals. Using the mean period of f_3 and f_5 for $k = 13$, the best-fit line has $\Delta\Pi_1^a = 38.1 \pm 0.3$ s and $\epsilon = 105 \pm 5$ s (Eq. 1). This is consistent with the value determined from the three significance tests applied directly to the period list, but the uncertainties are underestimated because they do not account for the m ambiguity. We assess our actual uncertainty by repeating fits to 1000 permutations of the periods, each time assigning every observed mode a random $m \in \{-1, 0, 1\}$ and then correcting to the intrinsic $m = 0$ value with an assumed rotational splitting

⁷ The error bars on the period measurements are much smaller than the points in Figure 4.

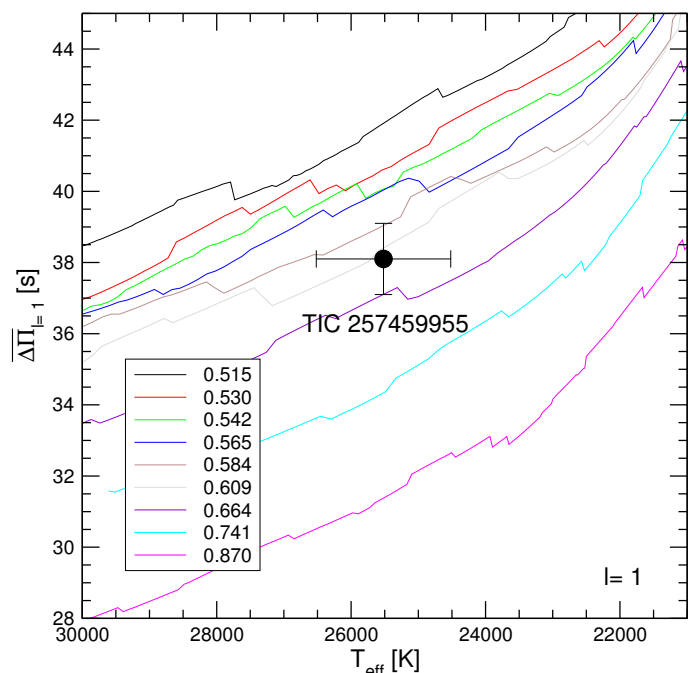


Fig. 6. Dipole ($\ell = 1$) average of the computed period spacings, $\overline{\Delta\Pi}_{\ell=1}$, assessed in a range of periods that includes the periods observed in TIC 257459955, shown as solid curves of different colors for different stellar masses. The location of TIC 257459955 is displayed with a black circle. We include the error bars associated to the uncertainties in $\Delta\Pi$ and T_{eff} . The stellar mass derived from linear interpolation is $M_{\star} = 0.621^{+0.057}_{-0.052} M_{\odot}$.

of either $f_3 - f_5$ or half that value. Some representative fits are shaded in the background of Figure 4. The standard deviation of best-fit slopes is 0.9 s, which we add in quadrature to the fit uncertainty for a final measured $\ell = 1$ asymptotic period spacing of $\Delta\Pi_1^a = 38.1 \pm 1.0$ s.

The middle panel of Figure 4 displays the residuals of the measured periods about this fit. We recognize an apparent oscillatory pattern in the residuals with a cycle length of $\Delta k \approx 6$, which could correspond to the mode trapping effect of “sharp” localized features in the stellar structure (as detected in other DBVs, e.g., Winget et al. 1994). These deviations from a strictly even period spacing may provide asteroseismic sensitivity to the location of the helium layer boundary or to chemical composition transitions in the core. The pulsation spectrum is displayed in units of period in the bottom panel of Figure 4, with the expected locations of the $\ell = 1$ modes for even period spacing indicated.

4.2. Analysis from the La Plata group

In our first analysis, we begin by assessing the stellar mass of TIC 257459955 following the methods described in several papers by the La Plata group on asteroseismic analyses of GV Vir stars and DBV stars (see, for instance, Córscico et al. 2007).

We first derive the “spectroscopic” stellar mass of TIC 257459955 from the T_{eff} and $\log g$ values and appropriate evolutionary tracks. We adopt the values $T_{\text{eff}} = 25,518 \pm 1000$ K and $\log g = 7.875 \pm 0.06$ from Voss et al. (2007)⁸, and employ the DB white dwarf evolutionary tracks from Althaus et al.

⁸ Note that we adopt uncertainties $\sigma_{T_{\text{eff}}} = 1000$ K and $\sigma_{\log g} = 0.06$ as nominal errors of T_{eff} and $\log g$.

(2009) produced with the LPCODE evolutionary code. These evolutionary tracks have been employed in the asteroseismic analyses of the DBV stars KIC 8626021 (Córscico et al. 2012), KUV 05134+2605 (Bognár et al. 2014), and PG 1351+489 (Córscico et al. 2014). The sequences of DB white dwarf models have been obtained taking into account a complete treatment of the evolutionary history of progenitor stars, starting from the zero-age main sequence (ZAMS), through the thermally pulsing asymptotic giant branch (TP-AGB) and born-again (VLTP; very late thermal pulse) phases to the domain of the PG 1159 stars, and finally the DB white dwarf stage. As such, they are characterized by evolving chemical profiles consistent with the prior evolution. We varied the stellar mass and the effective temperature in our model calculations, while the He content, the chemical structure at the CO core, and the thickness of the chemical interfaces were fixed by the evolutionary history of progenitor objects. In Figure 5 we show the evolutionary tracks along with the location of all the DBVs known to date. We derive a new value of the spectroscopic mass for this star on the basis of this set of evolutionary models. This is relevant because this same set of DB white dwarf models is used below to derive the stellar mass from the period spacing of TIC 257459955. By linear interpolation we obtain an estimate of the spectroscopic mass of $M_{\star} = 0.542^{+0.028}_{-0.025} M_{\odot}$.

In Section 4.1, we identified an incomplete dipole ($\ell = 1$) sequence of gravity modes with high radial order k (long periods) with consecutive modes ($|\Delta k| = 1$) that are nearly evenly separated in period by $\Delta \Pi_1^a = 38.1 \pm 1.0$ s. This follows our expectations from the asymptotic theory of non-radial stellar pulsations given by Eq. (1), where

$$\Pi_0 = 2\pi^2 \left[\int_{r_1}^{r_2} \frac{N}{r} dr \right]^{-1}, \quad (2)$$

N being the Brunt-Väisälä frequency, one of the critical frequencies of non-radial stellar pulsations. In principle, the asymptotic period spacing or the average of the period spacings computed from a grid of models with different masses and effective temperatures can be compared with the mean period spacing exhibited by the star to infer the value of the stellar mass. These methods take full advantage of the fact that the period spacing of DBV stars primarily depends on the stellar mass and the effective temperature, and very weakly on the thickness of the He envelope (see, e.g., Tassoul et al. 1990).

We assessed the average period spacings computed for our models as $\overline{\Delta \Pi_{\ell=1}} = (n-1)^{-1} \sum_k \Delta \Pi_k$, where the “forward” period spacing is defined as $\Delta \Pi_k = \Pi_{k+1} - \Pi_k$ (k being the radial order) for $\ell = 1$ modes and n is the number of theoretical periods considered from the model. The theoretical periods were computed with the LP-PUL pulsation code (Córscico & Althaus 2006). For TIC 257459955, the observed mode periods are $\Pi_k \in [245, 866]$ s. In computing the average period spacings for the models, however, we have considered the range [470, 1400] s, that is, we excluded short periods that are probably outside the asymptotic regime. We also adopt a longer upper limit of this range of periods in order to better sample the period spacing of modes within the asymptotic regime. In Figure 6 we show the run of the average of the computed period spacings ($\ell = 1$) in terms of the effective temperature for our DBV evolutionary sequences, along with the observed period spacing for TIC 257459955. As can be appreciated from the Figure, the greater the stellar mass, the smaller the computed values of the average period spacing. By means of a linear interpolation of the theoretical values of $\overline{\Delta \Pi_{\ell=1}}$, the measured $\Delta \Pi$ and spectroscopic effective temperature yield a stellar mass of

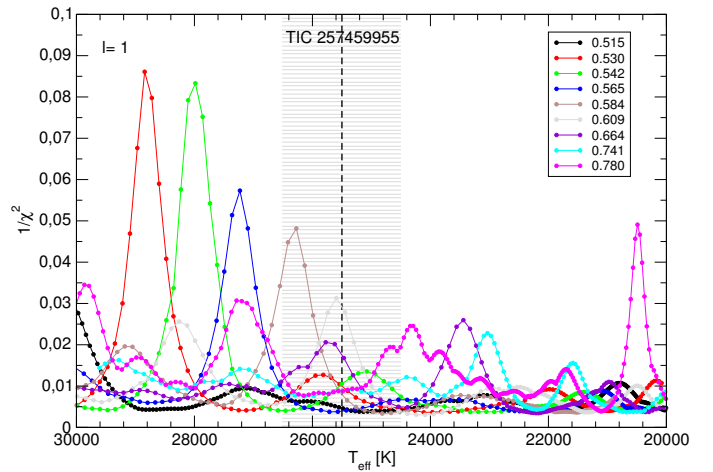


Fig. 7. Inverse of the quality function of the period fit in terms of the effective temperature for the case in which we assume that the modes are all $\ell = 1$. The vertical grey strip indicates the spectroscopic T_{eff} of TIC 257459955 and its uncertainties ($T_{\text{eff}} = 25\,518 \pm 1000$ K).

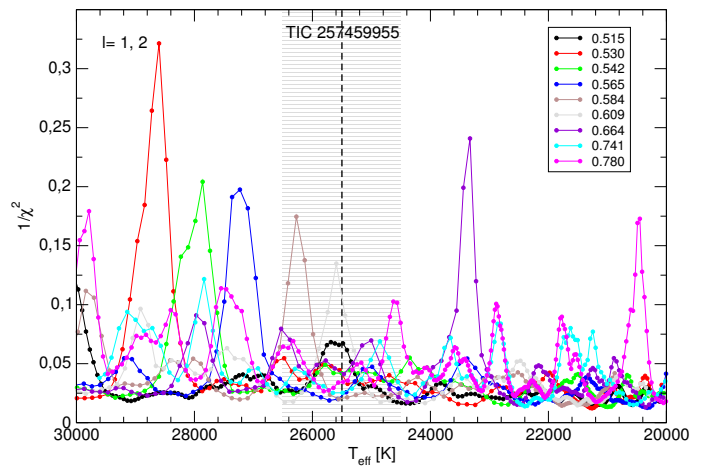


Fig. 8. Same as in Figure 7, but for the case in which we assume a mix of $\ell = 1$ and $\ell = 2$ modes.

$M_{\star} = 0.621^{+0.057}_{-0.052} M_{\odot}$. This stellar-mass value is higher than the spectroscopic estimate of the stellar mass.

On the other hand, if we instead fix the mass to the value derived from the spectroscopic $\log g$ ($0.542 M_{\odot}$), then we need to shift the model to higher effective temperature ($\approx 28,500$ K). This is the result we recover and refine in the period-to-period fitting. In this procedure we search for a pulsation model that best matches the *individual* pulsation periods of the star under study. The goodness of the match between the theoretical pulsation periods (Π_k^T) and the observed individual periods (Π_i^O) is assessed by using a merit function defined as:

$$\chi^2(M_{\star}, T_{\text{eff}}) = \frac{1}{m} \sum_{i=1}^m \min[(\Pi_i^O - \Pi_k^T)^2], \quad (3)$$

where m is the number of observed periods. The DB white dwarf model that shows the lowest value of χ^2 , if one exists, is adopted as the “best-fit model.” We assess the function $\chi^2 = \chi^2(M_{\star}, T_{\text{eff}})$ for stellar masses in the range $[0.515 M_{\odot} - 0.741 M_{\odot}]$. For the effective temperature we employ a much finer grid ($\Delta T_{\text{eff}} \sim 20$ K) which is given by the time step adopted in the evolutionary calculations of LPCODE. We assumed that the nine pulsation periods of TIC 257459955 (see Table 1) correspond to (i) modes with

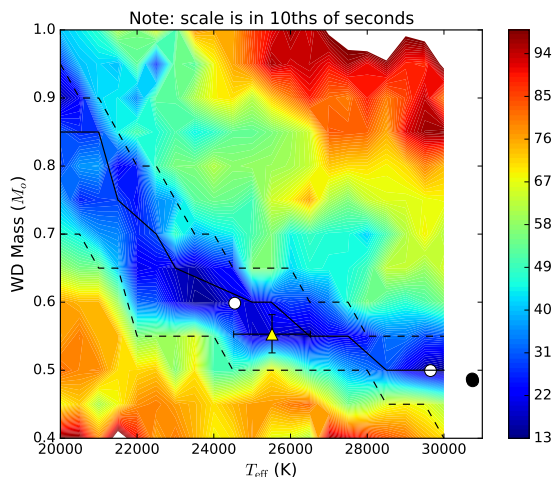


Fig. 9. Goodness-of-fit in the mass- T_{eff} plane for fit 4 (604 s mode is $m = 0$) in units of 10ths of seconds. The triangle is the location of the spectroscopic values, with error bars indicated. The white and black (colored for visibility) filled circles denote the location of the best fits listed in Table 3. The solid line is a line of constant period spacing at $\Delta P = 38.1$ s and the dashed lines show the 1-second “error bars” around that line.

$\ell = 1$ only, and (ii) a mix of $\ell = 1$ and $\ell = 2$ modes. The results are shown in Figs. 7 and 8, in which we depict the inverse of the quality function versus T_{eff} . Good period fits are associated with maxima in the inverse of the quality function. Unfortunately, there is no clear and unique solution in the range of effective temperatures from spectroscopy. However, a good solution is found at higher temperature for the stellar model with $M_{\star} = 0.530 M_{\odot}$ and $T_{\text{eff}} = 28,844$ K if all the periods are assumed to correspond to $\ell = 1$ modes. In the case in which the observed periods correspond to a mix of $\ell = 1$ and $\ell = 2$ modes, an excellent solution is obtained for a model with $M_{\star} = 0.530 M_{\odot}$ and $T_{\text{eff}} = 28,600$ K. The chemical profiles and Brunt-Väisälä frequency of the model corresponding to this last solution ($\ell = 1, 2$) are plotted in Figure 11 in the next section. If we assume that f_3 and f_5 are components of a rotational triplet (thus assuming that they are dipole modes), and consider the average of the periods at 597.6 s and 604.6 s in our procedure, then the period fits do not improve substantially, and still we can not find a robust asteroseismological solution compatible with the spectroscopic effective temperature of this star.

4.3. Analysis from the Texas group

The second asteroseismic fitting analysis that we performed uses models where the chemical profiles are parameterized, along with a few other properties. We used the WDEC (Bischoff-Kim & Montgomery 2018) with the parameterization of core oxygen profiles described in Bischoff-Kim (2018). In addition to the 6 core parameters and 5 parameters describing the helium chemical profile, we can also vary the mixing length coefficient α as well as the mass and effective temperature of the model. A 15th parameter sets the location of the base of the hydrogen layer, which is not relevant for DBVs.

We had to fix some parameters in order to keep the problem computationally tractable and also constrained. We fixed α to 0.96 (see Bischoff-Kim & Montgomery 2018) and some oxygen and helium profile parameters to values such that we reproduced profiles from Dehner & Kawaler (1995) and Althaus et al.

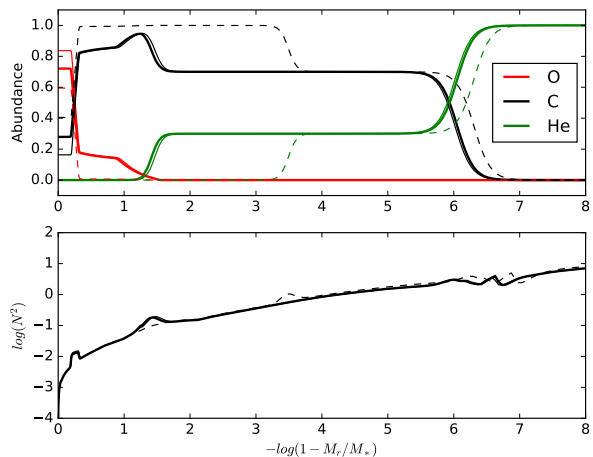


Fig. 10. Top panel: chemical abundance profiles for the best fit models of Table 3 (the three higher effective temperature fits 1, 3 and 4). The bold lines correspond to fit 1, while the thin solid lines correspond to fit 3. Fit 4 is represented by the thin dashed lines. Bottom panel: the corresponding Brunt-Väisälä frequency curves.

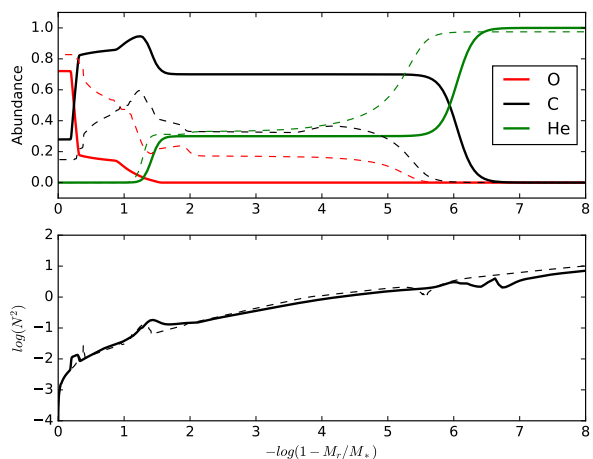


Fig. 11. Top panel: chemical abundance profiles for fit 1 of Table 3, as well as the best fit model of Section 4.2. The best fit model of Section 4.2 is represented by the dashed lines. We chose to contrast these two best fit models because of their similarities. Bottom panel: the corresponding Brunt-Väisälä frequency curves.

(2009). But we allowed three of the oxygen profile parameters (h_1 , h_2 , and w_1) to vary, as well as two of the helium profiles parameters (the location of the base of the helium envelope M_{env} and the pure helium layer mass M_{He}). In addition, we varied the mass and the effective temperature of the models, for a total of 7 parameters. These parameters were determined to be the ones that had the most effect on the quality of the fits.

We started our model comparison with a grid search to locate minima in the global parameter space. The values of the parameters calculated in our grid are listed in Table 2. In our comparison of the measured periods to the models, we considered three different values for the $m = 0$ component in the 598, 605 s multiplet: we tested each of these as the central component individually, as well as their average, which could be undetected between two observed $m = \pm 1$ modes.

Table 2. Parameters of the model grid used in the fits. For a description of each, see Bischoff-Kim & Montgomery (2018) and Bischoff-Kim (2018). For each parameter, we list the range followed by the step size.

Oxygen Profile	Helium Profile	Other
Grid parameters		
$h_1 = 0, 1; 0.1$	$M_{\text{env}} = 1.5, 10; 0.5$	$T_{\text{eff}} = 20, 000 - 30, 000; 500 \text{ K}$
$h_2 = 0, 1; 0.1$	$M_{\text{He}} = M_{\text{env}}, 10; 0.5$	$M_{\star} = 0.4, 1.0; 0.05 M_{\odot}$
$h_3 = 0.8; \text{fixed}$	$x_{\text{He}} = 0.3; \text{fixed}$	$\text{MLT } \alpha = 0.96; \text{fixed}$
$w_1 = 0.02, 0.52; 0.05$	$\alpha 1 = 16; \text{fixed}$	No hydrogen (M_H fixed to 20)
$w_2 = 0.15; \text{fixed}$	$\alpha 2 = 8; \text{fixed}$	
$w_3 = 0.36; \text{fixed}$		

Table 3. Best fit parameters, result of simplex search.

fit ($m = 0$ mode)	Stellar parameters		Envelope parameters		Core parameters			$1/\chi^2$ ($1/s^2$)	$\sigma_{\text{RMS}}(s)$
	$T_{\text{eff}}, M_{\star}$		$M_{\text{env}}, M_{\text{He}}$		h_1, h_2, w_1				
1 (598 s)	30737 K	$0.487 M_{\odot}$	1.505	6.158	0.721	0.246	0.370	14.2	0.283
2 (601 s)	24546 K	$0.598 M_{\odot}$	1.527	4.500	0.459	0.405	0.595	2.47	0.680
3 (601 s)	30749 K	$0.485 M_{\odot}$	1.555	6.124	0.837	0.217	0.381	1.73	0.813
4 (605 s)	29650 K	$0.499 M_{\odot}$	3.595	6.411	0.595	0.123	0.375	14.7	0.279

Table 4. List of periods for the best fit models. All modes are $\ell = 1$.

mode ID	k	observed period (s)	fit 1 (s)	fit 2 (s)	fit 3 (s)	fit 4 (s)
f_9	4	245.4399	245.5704	245.7442	245.1173	245.4326
f_4	10	485.5275	485.7931	486.3560	485.2120	485.5028
f_6	12	557.6493	557.3893	557.1444	556.9441	558.0835
f_3	13	597.5538	597.9700			
Inferred	13	601.1		602.0	599.4	
f_5	13	604.6423				604.1388
f_1	14	640.5330	640.5687	641.1684	640.7334	640.7684
f_2	15	678.4328	678.4701	678.0488	678.7829	678.2318
f_7	17	749.2676	748.9701	748.9309	749.7712	749.3228
f_8	20	865.9744	865.5980	865.1238	866.8779	865.9226
$\sigma_{\text{RMS}}(s)$			0.283	0.680	0.813	0.279

We finished with a simplex search (Nelder & Mead 1965) to refine the minima, calculating WDEC models on the fly as the algorithm sought to minimize σ_{RMS} . The simplex method explores the parameter space of the models on its own; it is not bound by the mass and effective temperature limits of our initial model grid, and in fact some of the best-fit models returned are hotter than 30,000 K. We list the parameters of the best fit models in Table 3, along with a measure of the quality of fit, computed the same way as in section 4.2 (Eq. 3) to facilitate comparison with the previous analysis. We also list a different measure of goodness of fit, the standard deviation σ_{RMS} , because that is the quantity minimized in our grid and simplex searches:

$$\sigma_{\text{RMS}} = \sqrt{\frac{m}{m-1}} * \chi^2 \quad (4)$$

where again, m is the number of observed periods. We list the periods of the best fit models in Table 4.

We show the best fit contour map for fit 4 (604 s mode is $m = 0$) in the mass vs. effective temperature parameter plane in Figure 9, along with the location of the best fits and lines of constant period spacing corresponding to the value derived from the period spectrum of the star. The contour plots for other $m = 0$ choices look similar. The period spacing for the models is calculated by fitting a line through the higher k modes ($k = 11$ and up) and determining the slope, in the same way we use the linear fit of Figure 4 to determine one value for the average

period spacing present in the pulsation spectrum of the star. The limit of $k = 11$ was chosen by visual inspection. Modes of higher radial overtone follow a linear trend closely, and so are reflective of the asymptotic period spacing discussed in section 4.1. The computation of period spacings for the models in the grid are further discussed in Bischoff-Kim et al. (2019). The correlation between the quality of fits and period spacing is striking. This is to be expected for this object with such a tight linear sequence of (assumed) $\ell = 1$ modes (Figure 4).

To determine the location of the spectroscopic point in Figure 9, we interpolated WDEC models to translate the $\log g$ of the star into a mass. We find $M_{\star} = 0.553^{+0.0287}_{-0.00274} M_{\odot}$, slightly different from the values inferred by the La Plata group. The discrepancy comes from the fact that surface gravity depends not only on the mass and effective temperature, but also on the interior structure of the models, and we use different models. The two best fits by a significant margin are fit 1 and fit 4. Both are at high effective temperature, inconsistent with the spectroscopic value. They differ mainly by the thickness of the helium envelope, M_{env} . Fit 1 agrees with the result that we found in Section 4.2. Considering that we base our fixed parameter values on models from that section, that is expected. In addition, we also have one good fit at lower effective temperature using the average of 598 and 605 s periods for $m = 0$ (fit 2), but it is not nearly as good of a fit. For completeness, we also list the best fit when choosing the 601 s mode as the $m = 0$ member of the triplet

at higher effective temperature (fit 3); in terms of properties of this model, it is essentially the same solution as fit 1, except the quality of the fit is not as good.

In Figs. 10 and 11, we show the chemical abundance profiles and Brunt-Väiäsälä frequency curves of the best fit models from Table 3, and contrast those fits with the results of Section 4.2. Fit 1 has similarities with the La Plata model, in the location of the transition zones. Those are mainly responsible for setting the period spectrum of a model so this is not by accident. In Fig 10 we note a possible manifestation of the core-envelope symmetry observed in the asteroseismic fitting of the DBV GD 358 and discussed in Montgomery et al. (2003). The two models differ in the location of bumps in their Brunt-Väiäsälä frequencies corresponding to the transitions from pure carbon to a mix of carbon and helium (at $\log(1 - M_r/M_\star) \simeq 1.5$ and $\log(1 - M_r/M_\star) \simeq 3.5$). The bumps have similar shapes. In the core-envelope symmetry, a feature in the core (or in this case deep in the envelope) can be replaced by a feature further out and produce a similar period spectrum. This will result in two models that fit almost equally well, or in this case a significant change in the location of a Brunt-Väiäsälä feature between best-fit models that use slightly different periods for the $k = 13$ mode. The central oxygen abundance and the transition from a mix of helium and carbon to pure helium have a weaker effect on the periods.

As mentioned in Section 4.1, the 598 s/604 s doublet is consistent with a rotationally split $\ell = 1$ mode. The rotation frequency Ω of the white dwarf is related to the frequency splitting $\Delta\sigma$ by a relation that involves the m identification of the mode and a mode dependent factor C_{kl} (Unno et al. 1989):

$$\Delta\sigma = m(1 - C_{kl})\Omega \quad (5)$$

For our best-fit model we find that the 598 s mode has $C_{kl} = 0.493$. Using that value and assuming one of the members of the doublet is the $m = 0$ mode, we find a rotation period of 7 hrs. If we have instead observed the $m = 1$ and $m = -1$ components of the triplet, then the rotation period is 14 hrs. Both are consistent with the rotation periods expected empirically for white dwarf stars (Kawaler 2015).

5. Discussion and conclusions

TESS observed the pulsating helium-atmosphere DBV white dwarf WD 0158–160 as TIC 257459955 for 20.3 nearly uninterrupted days in Sector 3 at the short 2-minute cadence. These data enabled accurate determination of the pulsation frequencies to $\sim 0.01 \mu\text{Hz}$ precision. Our frequency analysis reveals nine significant independent pulsation modes and eleven combination frequencies. The pattern of the observed pulsations is consistent with an incomplete sequence of dipole $\ell = 1$ modes with an asymptotic mean period spacing of 38.1 ± 1.0 s. Two modes separated by $19.6 \mu\text{Hz}$ could belong to a rotationally split $\ell = 1$ triplet, implying a stellar rotation period of 7 or 14 hours, depending on which components are being observed.

The shortest-period pulsation at 245 s was included in our frequency solution based on corroboration with archival photometry from Kilkenny (2016). It appears that a different set of modes were dominant in those ground-based observations that first revealed WD 0158–160 to be a DBV pulsator. Seasonal changes such as these have been observed in other DBVs such as GD 358 (e.g., Bischoff-Kim et al. 2019). The slight residuals in the periodogram of the fully prewhitened time series (Figure 2) near modes f_2 and f_8 likely indicate that these modes were varying in amplitude during the *TESS* observations.

Enabled by recent improvements in the WDEC (Bischoff-Kim & Montgomery 2018) and fostered by the collaborative TASC WG8.2, we present for the first time a direct comparison between asteroseismic analyses from the La Plata and Texas groups. A primary difference between the two sets of models is that La Plata group uses fully evolutionary models calculated with LPCODE, while the Texas group computes grids of structural models with parameters sampled on demand using WDEC. Both groups find that the measured mean period spacing of $\ell = 1$ modes trace paths of good model agreement of decreasing mass with increasing effective temperature (Figs. 6 and 9) that pass through the average DB white dwarf mass of $\approx 0.62 M_\odot$ (e.g., Kepler et al. 2019) at the spectroscopic effective temperature of $25,500 \pm 1000$ K from Voss et al. (2007).

When considering individual mode periods, both analyses achieve excellent asteroseismic fits to models with T_{eff} in excess of $\sim 29,000$ K and lower masses $M_\star \approx 0.5 M_\odot$. These solutions are significantly hotter than the spectroscopic effective temperature, but more in line with the spectroscopic surface gravity measurement. Uncertainties in T_{eff} measured from spectroscopy for DB white dwarfs in the DBV instability strip can be as high as ≈ 1000 K (as assumed in Section 4.2) due to large external errors (e.g., Beauchamp et al. 1999), and these best-fit seismic models might better represent the star WD 0158–160. Corrections for spectroscopically determined DB atmospheric parameters based on 3D convection simulations cannot account for this discrepancy (Cukanovaite et al. 2018). The only DBV with a reported effective temperature $> 30,000$ K is PG 0112+104 (Hermes et al. 2017a), with spectroscopic parameters $T_{\text{eff}} = 31,300 \pm 500$ K and $M_\star = 0.52 \pm 0.05 M_\odot$ (Dufour et al. 2010).

The structural profiles of the best-fit models from both analyses are compared in Figure 11. While at first glance, it might appear that there is little agreement, it is important to note that the transition zones (and the corresponding features in the Brunt-Väiäsälä frequency) do approximately line up. It is well known that pulsation periods are most sensitive to the location of the features in the Brunt-Väiäsälä frequency, and less so to their shape (e.g., Montgomery et al. 2003). The consistency of the results of the two seismic analyses is encouraging. Conducting these two analyses in parallel also helps us select a preferred best fit for the star.

We can convert the luminosities of our best-fitting models into seismic distances, which can be compared to precise astrometric distances from *Gaia*. The best-fit WDEC models 1, 3 and 4 in Table 3 have $T_{\text{eff}} = 30,750$ – $29,650$ K; the luminosity range is $\log L/L_\odot = -0.708$ to -0.795 , which implies a bolometric correction (B.C.; Koester 2018) of -3.22 to -3.11 magnitudes. We use the well-known formula $M_{V_\odot} - 2.5 \log(L/L_\odot) = M_V - \text{B.C.} = M_{\text{Bol},\star}$, where M_V is the absolute visual magnitude and M_{Bol} is the absolute bolometric magnitude. Using $M_{V_\odot} = 4.75$ and the apparent visual magnitude $m_V = 14.03$ for TIC 257459955, we obtain $M_{\text{Bol},\star} = 9.74$ to 9.85 . Applying the formula $5 \log d = M_{\text{Bol},\star}$ gives a distance of 68.6–72.1 pc. For the global best fits from both LPCODE and WDEC, we have $T_{\text{eff}} \approx 28,800$ K, $\log L/L_\odot \approx -0.867$, B.C. ≈ -3.06 . Using the above formulas produces an approximate distance of 64.7 pc. These seismic distances compare favorably with the *Gaia* DR2 (*Gaia* Collaboration et al. 2018) parallax-derived distance of 68.14 ± 0.28 pc from Bailer-Jones et al. (2018). We note that model 3 from Table 3 has a much lower luminosity $\log L/L_\odot = -1.258$, bolometric correction of 2.55 magnitudes, fainter $M_{\text{Bol},\star} = 10.45$ and closer distance of 52.0 pc, which disagrees with the *Gaia* DR2 value. These results demonstrate the value of the *Gaia* DR2 parallaxes to better determine the quality

of fits to stellar models, and suggest that model 4 from Table 3 has the best fit to the periods and parallax. These precise astrometric measurements should not be neglected in modern asteroseismic analyses.

The possibility that the nearby red dwarf G272-B2B is a common proper motion companion to WD 0158–160, as discussed by Kilkenny (2016), is also supported by the *Gaia* DR2 astrometry. At a distance of 68.58 ± 0.33 pc (Bailer-Jones et al. 2018), G272-B2B has $M_V = 9.29$, and using Table 15.7 in Drilling & Landolt (2000), this absolute magnitude is consistent with a type M1 dwarf, which is a bit more luminous than suggested by Kilkenny. With an on-sky separation of only $7''$ compared to the *TESS* plate scale of $22'' \text{pix}^{-1}$, G272-B2B will contribute significant light to the photometric aperture of TIC 257459955. In fact, the header keyword CROWDSAP from the PDC pipeline suggests that only 30% of the total flux originally measured in the aperture is from the white dwarf target WD 0158–160, which has the effect of decreasing the signal-to-noise of the periodogram by a factor of 1.8, potentially obscuring lower-amplitude pulsation signals.⁹

We note a striking similarity between the pattern of pulsation modes observed in TIC 257459955 and the prototypical DBV variable GD 358 (Winget et al. 1982). Over three decades of observations have revealed a clear pattern of nearly sequential $\ell = 1$ modes in GD 358 with a mean period spacing of 39.9 s (Bischoff-Kim et al. 2019). This is similar to the period spacing measured from the *TESS* observations of TIC 257459955, but the periods of the corresponding modes in GD 358 are all longer by ≈ 20 s. A comparative seismic analysis of these stars could reveal how this relative translation of mode periods results directly from small differentials in their physical stellar parameters.

The pulsation frequencies calculated for stellar models have azimuthal order $m = 0$, corresponding to the central components of rotationally split multiplets. Generally, not all components of a multiplet are detected in pulsating white dwarfs, and the observed modes are simply assumed to be $m = 0$ in the absence of other information. This can introduce discrete inaccuracies in the fitting of each period of a few seconds, compared to the millisecond precision that these periods are measured to from *TESS* photometry. The analysis from the Texas group (Section 4.3) demonstrated the non-negligible effect of this uncertainty for just a single radial order on the inferred stellar structure (Figure 11), treating each of f_3 , f_5 , and their average as the $m = 0$ mode. As a manifestation of a core-envelope symmetry, these small changes to a single mode period resulted in significant differences in the best-fit location of the base of the helium envelope. Metcalfe (2003) argued from Monte Carlo tests that fitting models with the assumption of $m = 0$ for modes detected from ground-based observations of DBVs yields the same families of solutions and often the same best-fit model (with root-mean-square period differences of ≈ 1 s) as when reliable m identifications are available; however, we should be wary of whether these results hold in the era of space photometry, as model fits are now being achieved to the unprecedented precision of our current period measurements (Giammichele et al. 2018).

Our interpretation of the detected signals from the *TESS* data did not consider their observed amplitudes. We identified the majority of peaks detected in the periodogram as nonlinear combination frequencies that appear at precise differences, sums, and multiples of independent pulsation frequencies (Table 1). These

combination frequencies are not comparable to calculations from stellar models and are important to identify and exclude from asteroseismic analyses. The amplitudes detected for the combination signals are expected to be much smaller than the independent pulsation mode amplitudes, and they are typically only detected for combinations of the highest-amplitude modes. We find an exception in the presence of a significant peak at the sum of the frequencies of two low-amplitude modes, f_4 and f_5 , suggesting that $f_4 + f_5$ may actually be an independent pulsation frequency that could improve our asteroseismic constraints. Still, there is less than a 0.5% chance of an independent mode coinciding this precisely with the sum of any nine other pulsation frequencies. We consider the risk of including a combination frequency in our model comparison much greater than the reward of an ostensibly better but possibly inaccurate fit. The peak at $f_4 + f_5$ would not have been adopted for exceeding our independent significance threshold regardless, and its inclusion as a combination frequency in our solution has a negligible effect on the period measurements for the independent modes. We do not consider the possibility that one of f_4 or f_5 may be a difference frequency involving the peak at $f_4 + f_5$, as these individually have higher observed amplitudes and match the pattern of mode frequencies expected from nonlinear pulsation theory.

We note an interesting possibility to test the hypothesis that individual peaks are consistent with combination frequencies based on their relative amplitudes. Wu (2001) provides analytical expressions for the amplitudes of combination frequencies that are based on a physical model for the nonlinear response of the stellar convection zone to the pulsations. This provides a framework for interpreting the amplitudes of combination frequencies in relation to their parent mode amplitudes that could constrain their spherical degrees, ℓ , and azimuthal orders, m (e.g., Montgomery 2005; Provencal et al. 2012). Besides resolving the common ℓ ambiguity when comparing measured to model mode periods, identifying non-axisymmetric modes ($m \neq 0$) would enable us to apply corrections to our measurements to recover $m = 0$ period estimates. This would alleviate the systematic errors from assuming $m = 0$ in the model fits, bringing the accuracy of our asteroseismic inferences closer to the level of precision that we currently achieve with the *TESS* data. Tools to constrain mode identifications in this way for space-based photometry of pulsating white dwarfs are currently in development.

This collaborative first-light analysis from TASC WG8.2 has demonstrated the quality of the *TESS* observations for measuring pulsations of DBV stars and the current state-of-the-art of their interpretation. *TESS* is continuing to observe new and known pulsating white dwarfs over nearly the entire sky, providing precise and reliable pulsation measurements for extensive asteroseismic study. Additional first-light papers from TASC WG8.2 on the pulsating PG 1159 star NGC 246 (Sowicka et al.) and an ensemble of DAV stars (Bognar et al.) are in preparation.

Acknowledgements. We thank TASC WG 8.2 for supporting this project and providing valuable feedback, especially D. Kilkenny and R. Raddi. ASB gratefully acknowledges financial support from the Polish National Science Center under project No. UMO-2017/26/E/ST9/00703. ZsB acknowledges the financial support of the K-115709 and PD-123910 grants of the Hungarian National Research, Development and Innovation Office (NKFIH), and the Lendület Program of the Hungarian Academy of Sciences, project No. LP2018-7/2018. This paper includes data collected with the *TESS* mission, obtained from the MAST data archive at the Space Telescope Science Institute (STScI). Funding for the *TESS* mission is provided by the NASA Explorer Program. STScI is operated by the Association of Universities for Research in Astronomy, Inc., under NASA contract NAS 5–26555. This work has made use of data from the European Space Agency (ESA) mission *Gaia* (<https://www.cosmos.esa.int/gaia>), processed by the *Gaia* Data Processing and Analysis Consortium (DPAC, <https://www.cosmos.esa.int/web/gaia/dpac/>

⁹ The PDC pipeline subtracts off the expected contributions from sources other than the target so that amplitudes measured for detected pulsations should be accurate (Twicken et al. 2010).

consortium). Funding for the DPAC has been provided by national institutions, in particular the institutions participating in the *Gaia* Multilateral Agreement.

References

- Althaus, L. G., Panei, J. A., Miller Bertolami, M. M., et al. 2009, *ApJ*, 704, 1605
- Althaus, L. G., Córscico, A. H., Isern, J., & García-Berro, E. 2010, *A&A Rev.*, 18, 471
- Astropy Collaboration, Price-Whelan, A. M., Sipőcz, B. M., et al. 2018, *AJ*, 156, 123
- Baran, A. S., Koen, C., & Pokrzywka, B. 2015, *MNRAS*, 448, L16
- Barentsen, G., Hedges, C., Vinícius, Z., et al. 2019, KeplerGO/lightkurve: Lightkurve v1.0b30, Zenodo: <https://doi.org/10.5281/zenodo.2611871>
- Bailer-Jones, C. A. L., Rybizki, J., Foesneanu, M., et al. 2018, *AJ*, 156, 58
- Beauchamp, A., Wesemael, F., Bergeron, P., et al. 1999, *ApJ*, 516, 887
- Bischoff-Kim, A. 2018, Zenodo. <http://doi.org/10.5281/zenodo.1715917>
- Bischoff-Kim A., Montgomery M. H., 2018, *AJ*, 155, 187
- Bischoff-Kim, A., Provencal, J. L., Bradley, P. A., et al. 2019, *ApJ*, 871, 13
- Bognár, Z., Pappáró, M., Córscico, A. H., Kepler, S. O., & Gyórfy, Á. 2014, *A&A*, 570, A116
- Brickhill, A. J. 1992, *MNRAS*, 259, 519
- Córscico, A. H., & Althaus, L. G. 2006, *A&A*, 454, 863
- Córscico, A. H., Althaus, L. G., Miller Bertolami, M. M., et al. 2019, arXiv e-prints, arXiv:1907.00115
- Córscico, A. H., Althaus, L. G., Miller Bertolami, M. M., & Bischoff-Kim, A. 2012, *A&A*, 541, A42
- Córscico, A. H., Althaus, L. G., Miller Bertolami, M. M., Kepler, S. O., & García-Berro, E. 2014, *J. Cosmology Astropart. Phys.*, 8, 054
- Córscico, A. H., Miller Bertolami, M. M., Althaus, L. G., Vauclair, G., & Werner, K. 2007, *A&A*, 475, 619
- Cox, J. P. 1984, *PASP*, 96, 577
- Cukanovaite, E., Tremblay, P.-E., Freytag, B., et al. 2018, *MNRAS*, 481, 1522
- Dehner, B. T., & Kawaler, S. D. 1995, *ApJ*, 581, L33
- Drilling, J. S. & Landolt, A. U. in Allen's *Astrophysical Quantities*, fourth edition, ed. A. N. Cox (New York, NY: Springer-Verlag), 381
- Dufour, P., Desharnais, S., Wesemael, F., et al. 2010, *ApJ*, 718, 647
- Dziembowski, W. 1977, *Acta Astron.*, 27, 203
- Fontaine, G., & Brassard, P. 2008, *PASP*, 120, 1043
- Gaia Collaboration, Brown, A. G. A., Vallenari, A., et al. 2018, *A&A*, 616, A1
- Gaia Collaboration, Prusti, T., de Bruijne, J. H. J., et al. 2016, *A&A*, 595, A1
- Giammichele, N., Charpinet, S., Fontaine, G., et al. 2018, *Nature*, 554, 73
- Handler, G., Pikall, H., O'Donoghue, D., et al. 1997, *MNRAS*, 286, 303
- Hermes, J. J., Gänsicke, B. T., Kawaler, S. D., et al. 2017b, *ApJS*, 232, 23
- Hermes, J. J., Kawaler, S. D., Bischoff-Kim, A., et al. 2017a, *ApJ*, 835, 277
- Kawaler, S. D. 2015, 19th European Workshop on White Dwarfs, 65.
- Kawaler, S. D. 1988, *Advances in Helio- and Asteroseismology*, 123, 329
- Kepler, S. O., Pelisoli, I., Koester, D., et al. 2019, *MNRAS*, 486, 2169
- Kilkenny, D. 2016, *MNRAS*, 457, 575
- Koster, D. 2018, private communication
- Metcalfe, T. S. 2003, *Baltic Astronomy*, 12, 247
- Montgomery, M. H. 2005, *ApJ*, 633, 1142
- Montgomery, M. H., Metcalfe, T. S., & Winget, D. E. 2003, *MNRAS*, 344, 657.
- Montgomery, M. H., & O'Donoghue, D. 1999, *Delta Scuti Star Newsletter*, 13, 28
- Nelder, J. A. & Mead, R. 1965, *The Computer Journal*, 7, 4, 308
- Newville, M., Otten, R., Nelson, A., et al. 2018, *lmfit/lmfit-py 0.9.12*, Zenodo: <http://doi.org/10.5281/zenodo.1699739>
- O'Donoghue, D. 1994, *MNRAS*, 270, 222
- Provencal, J. L., Montgomery, M. H., Kanaan, A., et al. 2012, *ApJ*, 751, 91
- Ricker, G. R., Winn, J. N., Vanderspek, R., et al. 2014, *Proc. SPIE*, 9143, 914320
- Stumpe, M. C., Smith, J. C., Van Cleve, J. E., et al. 2012, *PASP*, 124, 985
- Tassoul, M., Fontaine, G., & Winget, D. E. 1990, *ApJS*, 72, 335
- Twicken, J. D., Chandrasekaran, H., Jenkins, J. M., et al. 2010, *Proc. SPIE*, 77401U
- Unno, W., Osaki, Y., Ando, H., et al. 1989, *Nonradial oscillations of stars*.
- Voss, B., Koester, D., Napiwotzki, R., Christlieb, N., & Reimers, D. 2007, *A&A*, 470, 1079
- Winget, D. E., & Kepler, S. O. 2008, *ARA&A*, 46, 157
- Winget, D. E., Nather, R. E., Clemens, J. C., et al. 1994, *ApJ*, 430, 839
- Winget, D. E., Robinson, E. L., Nather, R. D., et al. 1982, *ApJ*, 262, L11
- Wu, Y. 2001, *MNRAS*, 323, 248
- Zacharias, N., Finch, C. T., Girard, T. M., et al. 2012, *VizieR Online Data Catalog*, 1322